JOURNAL OF GEOPHYSICAL RESEARCH, VOL. 115, B06102, doi:10.1029/2009JB006698, 2010

Crustal imaging of a mobile belt using magnetotellurics: An example of the Fowler Domain in South Australia

Stephan Thiel[1] and Graham Heinson[1]

Received 16 June 2009; revised 23 November 2009; accepted 3 December 2009; published 10 June 2010.

[1] A long-period magnetotelluric data set was obtained in 2005 along a two-dimensional profile across the western part of the late Archaean-early Proterozoic Gawler Craton, South Australia. The study is aimed at delineating the electrical conductivity structure of the crust and upper mantle underneath an east-west trending profile extending from the Gawler Range Volcanics in the east, crossing the Nuyts Domain and the highly prospective Meso-Proterozoic Fowler Domain, and terminating in the Eucla Basin to the west. The resistivity model shows a very electrically resistive crust and upper mantle underneath the Nuyts and Fowler Domain, possibly representing the cratonic root of the Gawler Craton extending to depths of ~160 km. The resistive cratonic root is closer to the surface underneath the Fowler Domain compared to the Nuyts Domain which supports findings from outcrops of metasediments of higher metamorphic grade in the Fowler Domain. A subvertical conductor marks the western terminus of the Fowler Domain and is imaged to upper mantle depths. On the eastern side of the Fowler Domain, another subvertical conductor extends to similar depths. These features spatially coincide with the Tallacootra and Coorabie shear zone at the surface, respectively, and their higher conductivity is likely due to a reduction in grain size of olivine associated with an increase in influence of grain boundary diffusion and thus enhanced conductivity. A comparison of the results with other surveys across mobile belts worldwide shows a more resistive response of the interpreted mobile belt of the Fowler Domain raising questions as to the nature of the domain.

Citation: Thiel, S., and G. Heinson (2010), Crustal imaging of a mobile belt using magnetotellurics: An example of the Fowler Domain in South Australia, *J. Geophys. Res.*, *115*, B06102, doi:10.1029/2009JB006698.

1. Introduction

[2] Archaean and Proterozoic Cratons, as well as their margins and surrounding mobile belts, have been the focus of a large number of interdisciplinary geoscientific surveys involving the magnetotelluric (MT) method [*Cagniard*, 1953]. For example, in North America, *Ferguson et al.* [2005] studied the Western Superior Province in Canada as part of the Lithoprobe project to map deeper structures of the granite-greenstone and metasedimentary belts and subprovinces. *Evans et al.* [2005] report an electrically resistive Archaean Rae Craton, Canada, bounded by a more conductive belt (Piling Group). In India, a similar electrical response has been reported by *Harinarayana et al.* [2006], with the Archaean Dharwar Craton being resistive and the Southern Proterozoic granulite terranes being more conductive. Economic resources such as diamond and gold occurrences in the mobile belts surrounding the South African Kaapvaal Craton are another incentive to pursue the understanding between surface expressions of Archaean subdomains and the deep crust/upper mantle underneath [*Hamilton et al.*, 2006]. Magnetotelluric surveys conducted in Namibia describe enhanced conductivity due to possible graphite enrichment in shear zones within the Damara mobile belt between the Congo and Kalahari Cratons [*Ritter et al.*, 2003].

[3] Central and western Australia is composed of numerous Archaean to Proterozoic cratons that had accreted to form a single continent by the Meso-Proterozoic [*Betts et al.*, 2002]. South Australia is dominated by the Archaean to Palaeoproterozoic Gawler Craton [*Daly et al.*, 1998] (Figure 1). Although different geological domains have been identified within the Gawler Craton (Figure 1), its overall tectonic evolution and the relationships between these domains are very poorly understood, due largely to extensive cover of younger sediments. In many cases the geological domains and their associated boundaries have been defined purely through interpretations of potential field data. MT is ideal for investigating the structure of the Gawler Craton due to its ability to penetrate sedimentary cover and to image lithospheric-scale features, as well as the absence of cultural electrical noise throughout most of the craton.

[1]Tectonics, Resources and Exploration, School of Earth and Environmental Sciences, University of Adelaide, Adelaide, South Australia, Australia.

0148-0227/10/2009JB006698

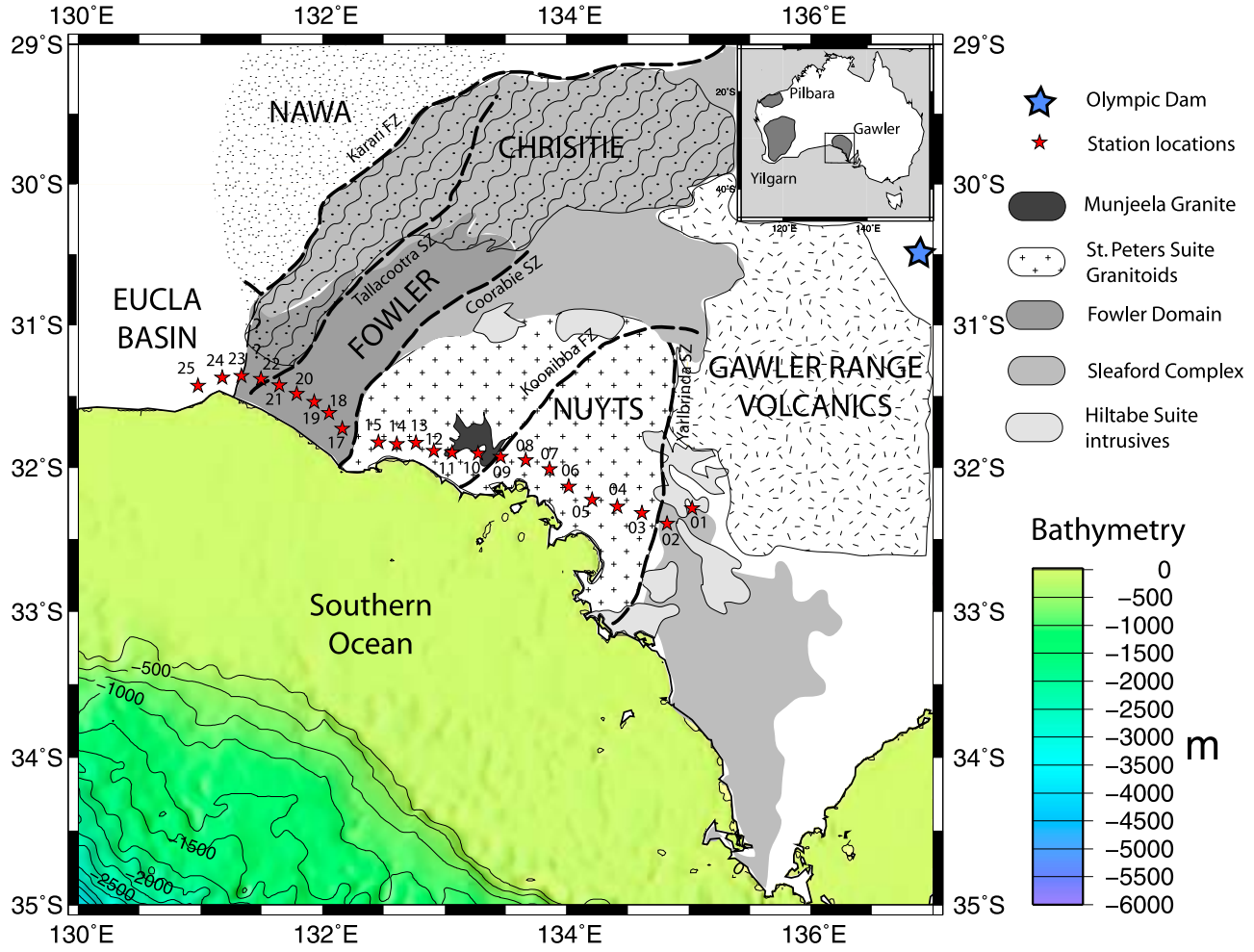

Figure 1. Long-period MT stations on top of the regional geology map of the field area and shaded bathymetry relief of the Southern Ocean. The profile extends over 400 km, crossing the Nuyts and Fowler Domains and numerous major framework shear zones, which are part of the Gawler Craton. The passive continental margin is relatively wide with the bathyal zone approximately 150–200 km away from the coast. FZ is fault zone and SZ is shear zone.

Three major events have defined the present-day architecture of the Gawler Craton, the oldest being the late Archaean to Palaeoproterozoic Sleafordian Orogeny (2440–2400 Ma), followed by the Palaeoproterozoic Kimban Orogeny (1730–1690 Ma), the Mesoproterozoic Karari Orogeny (1570–1540 Ma), and the Coorabie Orogeny (1470–1450 Ma) [*Teasdale*, 1997; *Swain et al.*, 2005b; *Direen et al.*, 2005; *Swain et al.*, 2005a; *Fraser and Lyons*, 2006; *Hand et al.*, 2007].

[4] The Gawler Craton is not only interesting from a tectonic point of view, but it has also generated a substantial economic interest. It hosts numerous mineral deposits of which the iron oxide copper-gold Olympic Dam deposit is the world's largest uranium producer [*Hitzman et al.*, 1992]. The Olympic Dam deposit is situated along the eastern margin of the Gawler Craton and MT studies show a zone of enhanced conductivity connecting the deposit with the lower crust, suggesting upward movement of CO_2-bearing volatiles followed by precipitation of graphite along grain boundaries [*Heinson et al.*, 2006]. The MT survey presented here is designed to investigate the electrical structure of the Fowler Domain and the Nuyts Domain, which are situated on the western side of the Gawler Craton, and of the major shear zones which act as bounding structures. The Fowler Domain, also referred to as Fowler Orogenic Belt or Fowler Suture Zone [*Daly et al.*, 1998], is poorly outcropping and aeromagnetic images show northeast trending magnetic highs that are separated by shear zones (Figures 1 and 2) [*Thomas et al.*, 2008].

2. Geological Setting

[5] The Fowler Domain and the Nuyts Domain form part of the late Archaean-Mesoproterozoic metasedimentary and metaigneous Gawler Craton (Figure 1). The tectonic history of the Gawler Craton is complex and characterized by multiple orogenies and exhumation events [*Teasdale*, 1997; *Swain et al.*, 2005a, 2005b; *Payne et al.*, 2006]. The oldest nuclei of the craton comprise the Archaean Mulgathing and Sleaford Complexes [*Swain et al.*, 2005b].

[6] After a period of 400 million years of no tectonic activity, Proterozoic events between 2000 and 1500 Ma

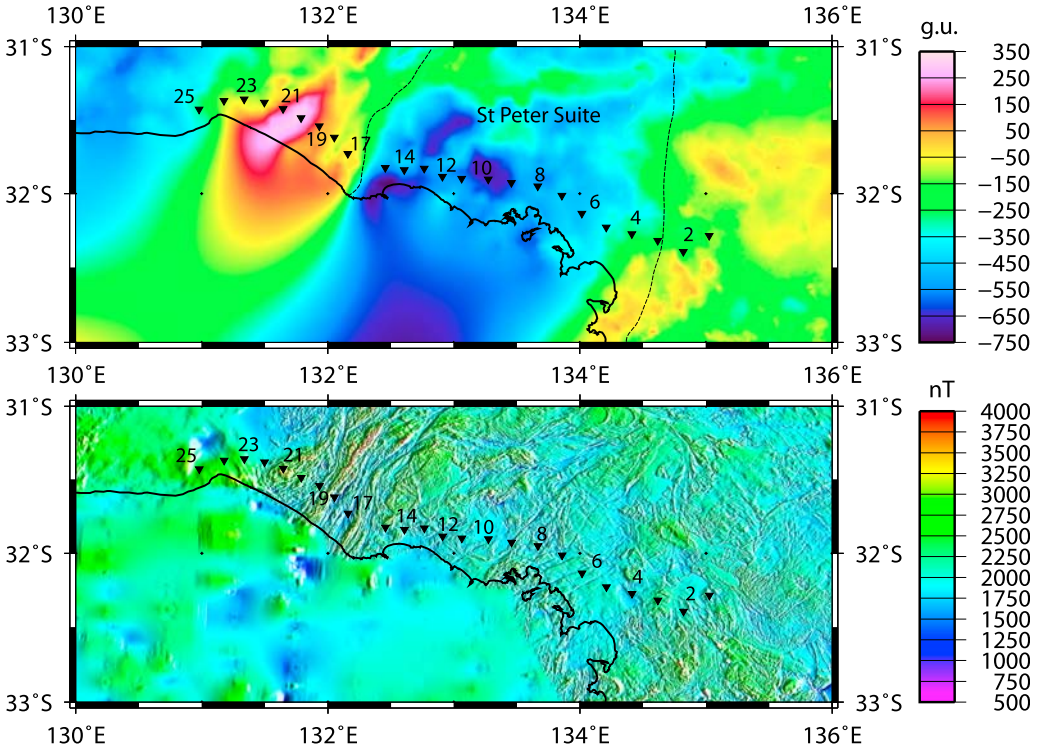

Figure 2. MT stations superimposed on (top) gravity and (bottom) total magnetic intensity image of the survey area. The Nuyts and Fowler Domain show distinctively different gravity and magnetic responses due to the magmatic emplacement of the St. Peter Suite of the Nuyts Domain versus the shear zone-intersected Fowler Domain.

have largely shaped the Gawler Craton as seen today. In this time span, sedimentary processes appear to dominate in the 2000–1690 Ma interval and are followed by dominantly magmatic processes during 1690–1500 Ma [*Hand et al.*, 2007]. During the 2000–1690 Ma interval a number of large rift basins developed across the Gawler Craton. The deposited sedimentary basins have bimodal magmatic suites associated with them. The Fowler Domain contains both pelitic metasediments [*Daly et al.*, 1998] and 1726 ± 9 Ma old mafic metagabbros [*Fanning et al.*, 2007]. The 1730–1690 Ma Kimban Orogeny had a profound metamorphic influence on deposited metasediments and metamorphism reached amphibolite facies in the Fowler Domain [*Teasdale*, 1997].

[7] At 1630 Ma the alkaline, porphyritic rhyodacite of the Nuyts Volcanics erupted and were subsequently intruded by the 1620–1608 Ma St. Peter Suite [*Flint et al.*, 1990; *Swain et al.*, 2008]. Recent results of geochemical analysis reveals characteristics of subduction-related arc magmatism of the St. Peter Suite and suggests variable recycling of crust-derived sediment. *Swain et al.* [2008] propose that south-dipping subduction terminated at 1608 Ma and subsequently migrated north to form the Musgrave magmatic arc. Almost contemporaneously, a major tectonothermal event is suggested at 1600 Ma in the western part of the Fowler Domain based on new thermobarometric and geochronological data [*Thomas et al.*, 2008]. The event resulted in lower crustal high-grade and midcrustal amphibolite-grade metamorphism. Between 1595 and 1575 Ma a large-scale magmatic event formed the Hiltaba Suite and the Gawler Range Volcanics (GRV) and form one of the largest felsic volcanic systems in the world [*Daly et al.*, 1998]. The GRV have a maximum thickness of about 1.5 km. The Hiltaba Suite comprises strongly fractionated granites to granodiorites (>70 wt% SiO_2, which consist of more mantle-derived material than the host rock in which they reside [*Stewart and Foden*, 2003]. The GRV and Hiltaba Suite are possibly part of a back-arc setting of a margin associated with the Musgrave magmatic arc.

[8] At 1585 Ma the St. Peter Suite was subsequently intruded by the unfractionated Munjeela Granite, as indicated by potential field data (see Figure 2). The Coorabie Orogony between 1550 and 1450 Ma is believed to have reactivated major northeast trending shear zones, e.g., the Tallacootra and Coorabie shear zone, which bound the Fowler Domain to the west and east, respectively [*Direen et al.*, 2005; *Swain et al.*, 2005a; *Fraser and Lyons*, 2006]. Furthermore, the Karari fault zone in the northwestern part of Gawler Craton also underwent reactivation during this period. Following this active period was a time of tectonic quiescence with deposition of sediments in the Neoproterozoic and Cenozoic [*Parker*, 1993].

2.1. Shear Zones

[9] Shear zones form an important link between the histories of different subdomains within the Gawler Craton and hold important information about the architecture of orogenic belts. There are three major generations of shear zones that have been recognized across the Western Gawler Craton [e.g., *Teasdale*, 1997]: (1) (SZ_1) east-west trending

shear zones, which are largely parallel to the survey line; (2) north-east trending craton-scale shear zones (SZ_2), dominating the geology of the Western Gawler Craton (e.g., Tallacootra and Coorabie SZ); (3) the Karari Fault Zone (SZ_3). The tectonic events resulting in the SZ_2 shear zones also caused the emplacement of the 1540 Ma granulites and the 1490 Ma amphibolites and pegmatites in the Fowler Domain, as well as the 1590 Ma Hiltaba intrusives. The northeast trending shear zones coincide with low-intensity magnetic anomalies (Figure 2) and form the Fowler Belt extending to 200 km width at the intersection with the survey line. The Coorabie Shear Zone represents the easternmost SZ_2 shear zone and separates the Fowler Domain in the west from the Nuyts Domain to the east. The Coorabie Fault and the Colona Fault form the easternmost and westernmost boundaries of the Coorabie Shear Zone, respectively [*Parker*, 1993]. Another major SZ_2 shear zone is the high-grade mylonitic Tallacootra Shear Zone which extends over 700 km and forms the western boundary of the Fowler Domain. New $^{40}Ar/^{39}Ar$ data of the major framework shear zones suggest a single fault system comprising the Tallacootra, Coorabie, and Karari shear zones between 1460 and 1440 Ma and possible earlier metamorphism and deformation between ≈1530 and 1550 Ma [*Fraser and Lyons*, 2006]. Reshuffling of already adjacent crustal blocks is therefore more likely than a composition of far-away terranes [*Fraser and Lyons*, 2006]. *Direen et al.* [2005] reports sinistral strike-slip offset of tens of kilometers. Gravity forward modeling suggests a 70° dip to the northwest of the major framework shear zones, with penetration depths of at least 15 km.

[10] The SZ_3 Karari Fault Zone postdates all SZ_2 shear zones and is characterized by a significant high-intensity magnetic anomaly. It truncates the SZ_2 shear zones to the west and north. There are no known outcrops of the Karari Fault Zone and only two drill cores have intersected it.

2.2. Potential Field Data Signatures

[11] Total magnetic intensity (TMI) maps of the region show a set of anastomosing demagnetized shear zones oriented northwest-southeast in the Fowler Domain (Figure 2). The shear zones are separated by highly magnetized blocks (~2000 nT). The shear zones show cross-cutting by granitoid plutons in places. The high gravity response of up to 350 g.u. of the Fowler Domain is largely due to the dense metasediments. The Coorabie shear zone (cf. Figure 1) marks the eastern boundary of the gravity high and the Nuyts Domain to the east is largely represented by less dense St. Peter Suite granitoids (~−400 g.u.). The low-density Munjeela Suite granites intrude near site 10 and have a relatively low gravity response of ~−750 g.u. The TMI image shows a homogeneous response for the Munjeela granite situated just west of the Koonibba fault zone (cf. Figures 1 and 2).

3. MT Data

[12] In 2005, long-period MT data were recorded at 24 stations, sites 01–25 (site 16 did not record), along an approximately 450 km long transect from ESE to WNW following the only highway that runs east-west and crossing the major shear zones at approximately right angles (Figure 1). The MT profile extends from the GRV in the east, across the Nuyts Domain comprising the granite-diorite St. Peter Suite in the center (stations 03–15) to the Fowler Domain to the west (stations 17–21). Stations 22 to 25 cover the adjacent sedimentary Eucla Basin with thicknesses up to 3 km, which are expected to have an inductive effect due to the lower resistivity of the sediments. Stations 1–10 have an approximate spacing of 20 km, which was reduced to 15 km across the western part of the Nuyts Domain and the Fowler Domain for stations 11–25. This was to reach a compromise between covering the main domains and to ensure enough spatial resolution for middle to upper crustal structures. Hiltaba Suite granites 1600–1585 Ma of age crop out near site 01 and 02 at the boundary between the Nuyts Domain and GRV (Figure 1). The Munjeela Granites intrude the St. Peter Suite between sites 09 and 11 within the Nuyts Domain. The long-period MT instruments, developed by Adelaide University, recorded data at 10 Hz, averaged and downsampled into blocks of 1 s giving responses between 10 and 6000 s. Each station recorded two horizontal components of the electric field (E_x, E_y with x north and y east) and three components of the magnetic field (H_x, H_y, H_z) for around 70 h. All time series data were processed using a robust remote reference code [*Chave et al.*, 1987; *Chave and Thomson*, 1989] and produced MT impedances $\boldsymbol{Z} \in \mathbb{C}$ and geomagnetic transfer functions $\boldsymbol{T} \in \mathbb{C}$.

$$\begin{pmatrix} E_x \\ E_y \\ H_z \end{pmatrix} = \begin{pmatrix} Z_{xx} & Z_{xy} \\ Z_{yx} & Z_{yy} \\ T_{xz} & T_{yz} \end{pmatrix} \begin{pmatrix} H_x \\ H_y \end{pmatrix} \tag{1}$$

Most of the time, two or three stations recorded simultaneously to allow remote-referencing where necessary [*Gamble et al.*, 1979]; however, coherence thresholding of single-site data with a higher cutoff produced better results in some cases. Geomagnetic declination of the survey area lies between 5° and 6° and has been corrected for, so that the x and y coordinates denote geographic north and east, respectively. Apparent resistivity and phases were calculated from MT impedance components (Figure 3). Stations commonly show a split in the phases and apparent resistivities at around 200 s, even more so for stations 8–24. The yx components of the impedance tensor decrease in apparent resistivity and increase in phase across all stations, which is most likely the result of the inductive ocean. Static shift is most prominent for stations 1–13 with almost equal phases and a similar shape in the resistivity curves of the xy component.

3.1. Induction Arrows

[13] Induction arrows show the regional resistivity distribution without being affected by static shift as the MT impedance [*Jones*, 1988] but are primarily sensitive to only lateral resistivity variations. In the Parkinson convention, used here, real arrows will point away from resistive blocks and toward zones of higher conductivity. Figure 4 illustrates the real components of the induction arrows for three different periods, where small periods (high frequencies) indicate influences of shallow and local structures and longer periods display the influence of the regional and deep resistivity distribution. Figure 4 also shows phase

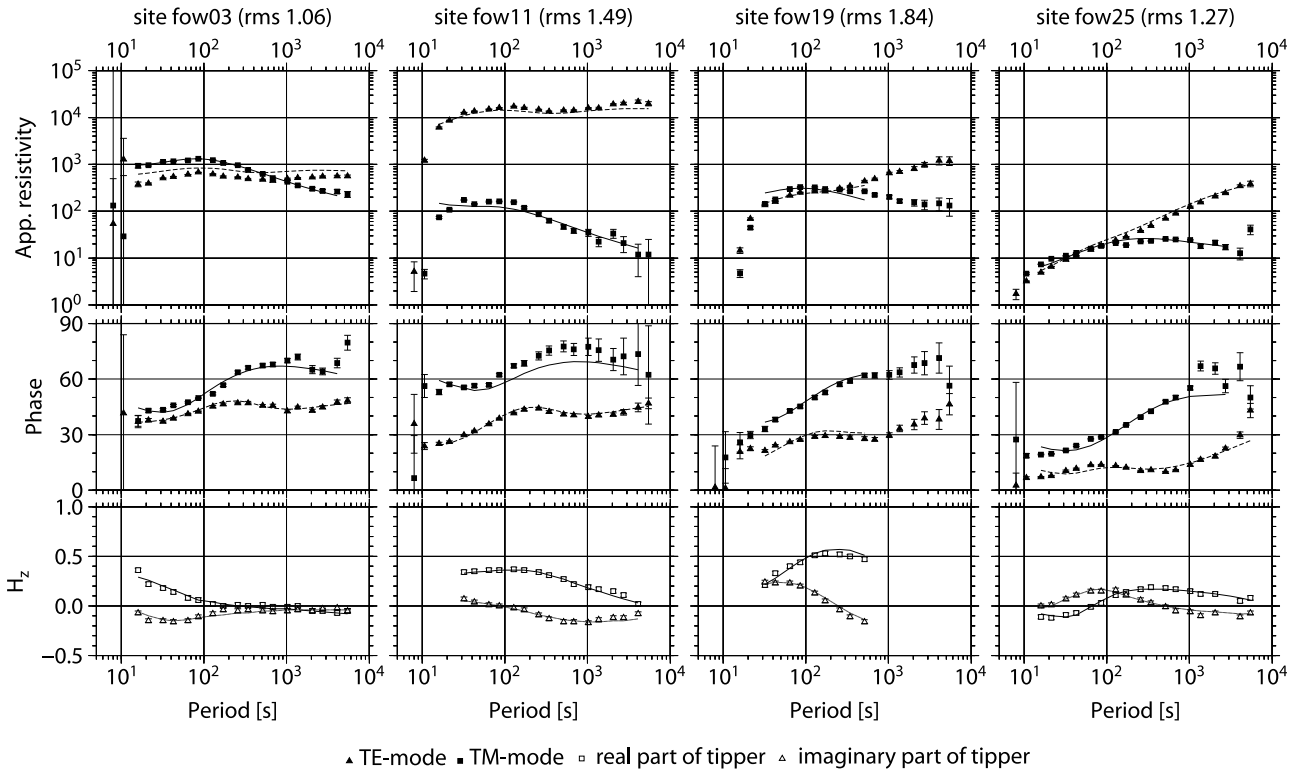

Figure 3. Apparent resistivity ρ_a, phase Φ, and tipper $\boldsymbol{T}$ plots for four selected stations representative for their respective geological domains and adjacent sites. Solid and dashed lines represent the modelled responses of the resistivity profile in Figure 11.

tensor ellipses, which indicate direction of current flow along the main axes of the ellipses. The ellipses are shaded according to the minimum phase [*Caldwell et al.*, 2004] and indicate the change of resistivity with depth, e.g., low phases correspond to an increase in resistivity toward longer periods and hence greater depths [*Simpson and Bahr*, 2005].

[14] At a period of 42 s, real induction arrows are large and point consistently southwest. Exceptions are stations 01–04, where the magnitude of the arrows is smaller, presumably due to the longer distance of the stations to the ocean. Stations 20–24 show a 90° deflection of the real arrows, indicating a north-south trending resistivity interface between station 22 and 23; this possibly represents the margin of the Gawler Craton. Arrows are generally larger for stations 16–21, corresponding to the Fowler Domain, and decrease in size across the St. Peter Suite (stations 4–15). These two domains also correspond spatially to areas of gravity highs and lows, respectively (Figure 2). For 682 s period, the magnitude of the arrows decreases and arrows in the western part of the profile rotate by about 20° toward the conductive boundary near station 22. Arrows rotate again toward the ocean for long periods (e.g., 2730 s) due to the conductive deep seawater located approximately 150–200 km to the south.

[15] To summarize, arrows show some variation in the orientation across the profile and are influenced by the continental shelf/conductor and the deep sea from shorter to longer periods. Imaginary components of the arrows, not shown here, are mostly parallel to the orientation of the real arrows for 682 s, indicating two-dimensionality. However, for periods of 2730 s some imaginary arrows at the western part of the profile are no longer parallel suggesting three-dimensionality.

4. Effects of Sedimentary Basins and the Ocean

[16] As discussed above, the induction arrows corresponding to the observed electromagnetic fields show a general SW-oriented deflection across the profile line with rapid changes in orientation and magnitude between stations 20 and 25 (Figure 5). Therefore conductive features responsible for the deflection cannot be assumed to solely lie directly beneath the profile. In order to quantify this effect, we have modeled a priori information using a 3-D finite difference forward modeling code [*Mackie et al.*, 1993], e.g., the ocean using bathymetry data by *Smith and Sandwell* [1997] and Depth to Proterozoic basement maps indicating sediment basin thicknesses.

[17] The resistivity of the ocean has been set to 0.33 Ωm −1 while we assign a sediment resistivity of 20 Ωm m−1. The sediment thicknesses reach more than a kilometer beneath stations 23–25 and also underneath the slopes of the passive continental margin and the abyssal plains. However, the forward model requires a fairly high (1000 Ωm m−1) half-space resistivity in order to explain the long induction arrows. Tests with a 100 Ωm m−1 half-space cannot reproduce the magnitude of the arrows. Figure 5 shows that the over-all trend of the observed arrows can be recovered using the a priori information in the forward model. The north-south trending sediment packages of the Eucla Basin

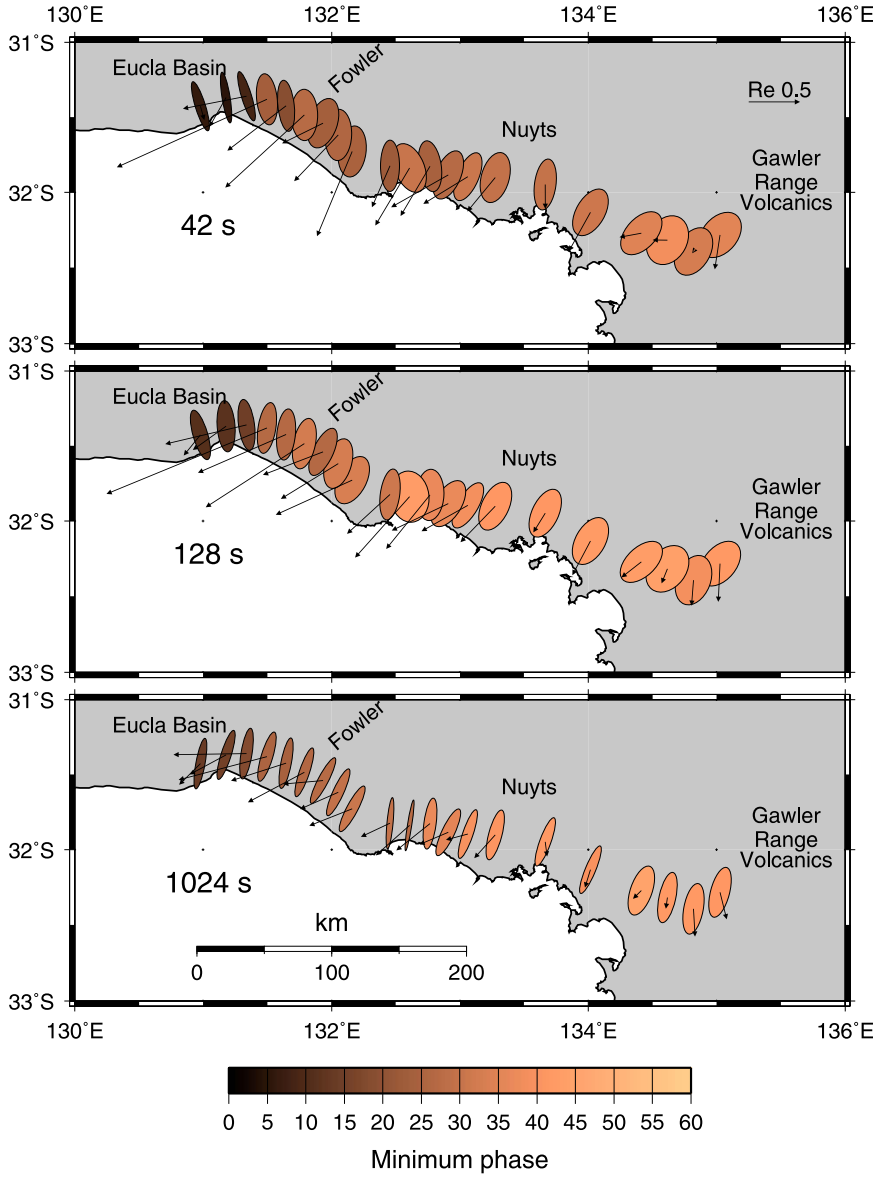

Figure 4. Phase tensors and real induction arrows for 42, 128, and 1024 s. Phase tensor ellipses have been shaded according to minimum phase value. Localities are tsz, Tallacootra Shear Zone; clfz, Colona Fault Zone; crfz, Coorabie Fault Zone; kfz, Koonibba Fault Zone; ysz, Yarlbrinda Shear Zone.

(Figure 6) are largely responsible for an increase in magnitude and a westward deflection in the orientation of the real arrows for stations 17–23 in the period range between 5 s and hundreds of seconds. Responses of other forward models (not shown) included meshes which constrained the conductivities at depths larger than 410 km to less than 10 Ωm m−1 [*Xu et al.*, 1998]. Those models resulted in smaller induction arrows for periods longer than 100 s and would have thus required even higher resistivities than 1000 Ωm m−1 of the half-space to reproduce the observed arrow magnitudes.

[18] The forward model cannot reproduce the large arrows for periods longer than 500 s in the observed data, suggesting a deeper nonsedimentary conductor underneath stations 22–25. Furthermore, the variability in both the orientation and magnitude of the arrows across the profile also highlights that there are other structural changes along the profile, which have not been accounted for in the forward model. Nevertheless, most of the deflection in the induction arrows can be readily explained by factoring in the conductive ocean and sediments.

[19] Given the geometry of the above-mentioned conductive ocean relative to the profile line, a strong resistivity interface south of the profile would also cause charge accumulation, which affects the electric field. This effect is known as static shift [*Jones*, 1988] and results in a constant offset in the observed apparent resistivities ρ_a for the mode with currents crossing the boundary perpendicular. In our case, we would expect such an offset primarily for the mode with the electric field aligned north-south.

[20] Figure 7 illustrates the apparent resistivities and phases for sites 01–12. The TE mode (currents perpendic-

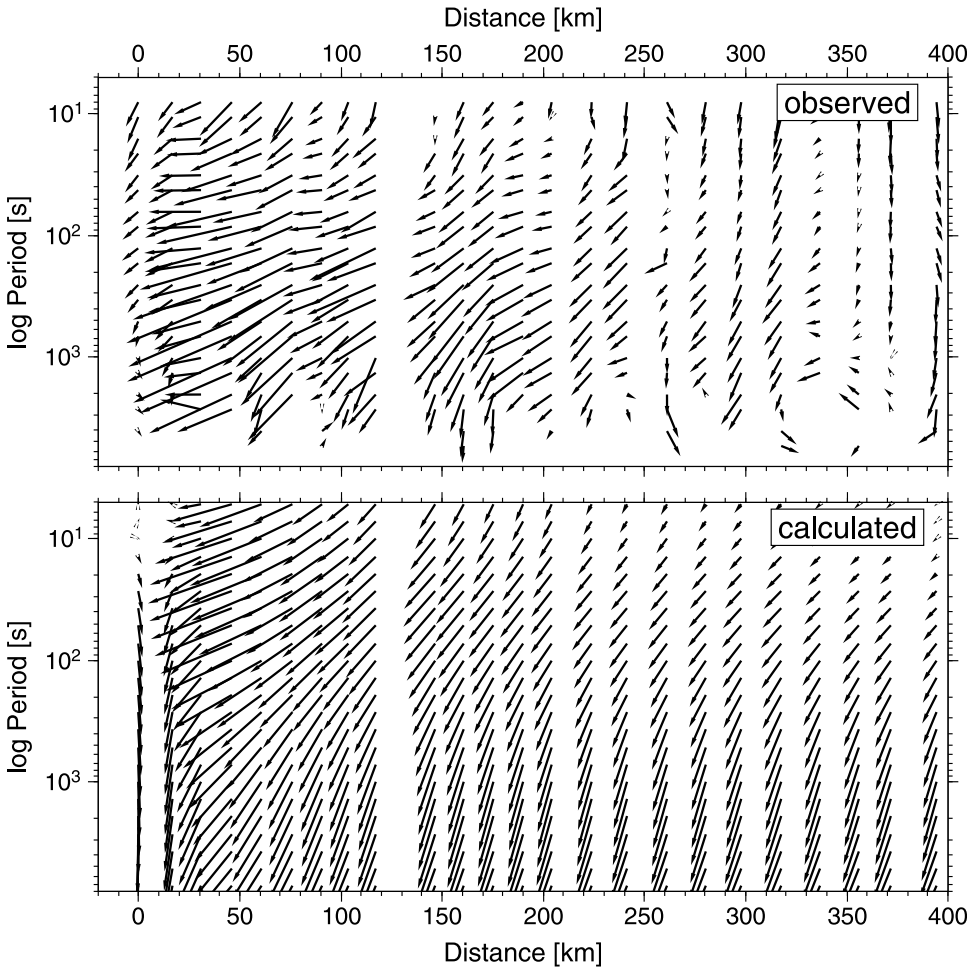

Figure 5. Comparison of the observed and calculated real induction arrows. Inclusion of the sedimentary basins and the ocean to the south of the profile explains the main trend of the southwest orientation of the real induction arrows. Observed induction arrows show a larger variability due to heterogeneous subsurface structure.

ular to profile and coast line) exhibits small variability in the phases for all 12 sites with less than 10° spread for periods longer than 50 s. Corresponding apparent resistivities vary by more than two orders of magnitude. In contrast, the TM mode apparent resistivities vary by just over one order of magnitude for the 12 easternmost sites considered here, while the corresponding TM mode phases show a spread of up to 30°. This indicates that the TE mode apparent resistivities are affected by static shift, while the TM mode is not so much affected by the galvanic offset. There is some correlation between the static offset to higher apparent resistivities toward the western sites, which are closer to the land/ocean boundary. Stations 13–25 are not included in Figure 7 since the western sites are also affected by the north-south trending sedimentary basins (cf. Figure 6) and the likely deeper conductor underneath the western stations. Given the geometry and relative position of those features in relation to the profile suggests that static shift effects could occur in both modes for some of the western stations.

[21] In addition to the static offset in the TE mode the inductive effect of the ocean and conductive sediments to the south cannot be fully discarded. Within the ocean, large current systems will flow parallel to the profile of measurement causing a small but measurable inductive effect [*Simpson and Bahr*, 2005]. As mentioned above, the induction arrows indicate inductive effects of the ocean, especially for sites near the coast, and perhaps more importantly near the abyssal plains some 200 km away. A quantification of the inductive effect is illustrated in Figure 8, for a forward model incorporating the ocean (0.33 Ωm m−1) and sediments (20 Ωm m−1) using the code of *Mackie et al.* [1993]. In anticipation of the model in Figure 11, we have included a conservative two-layered model with a resistivity of 50 Ωm m-1 for the top 5 km and 10,000 Ωm m−1 below. The values are chosen somewhat arbitrary, but the resistive crust and mantle should reflect typical resistivity values of Archaean lithosphere [*Jones et al.*, 2001; *Spratt et al.*, 2009], overlain by younger and more porous rocks in the top 5 km. The responses illustrate a downward bias in the phases of the TE mode for periods longer than about 500 s, which results in an overestimation in the apparent resistivities (Figure 8) compared to a remote site about 500 km away from the coast (marked in blue in Figure 8). The TM mode is not as severely affected by the conductive ocean/

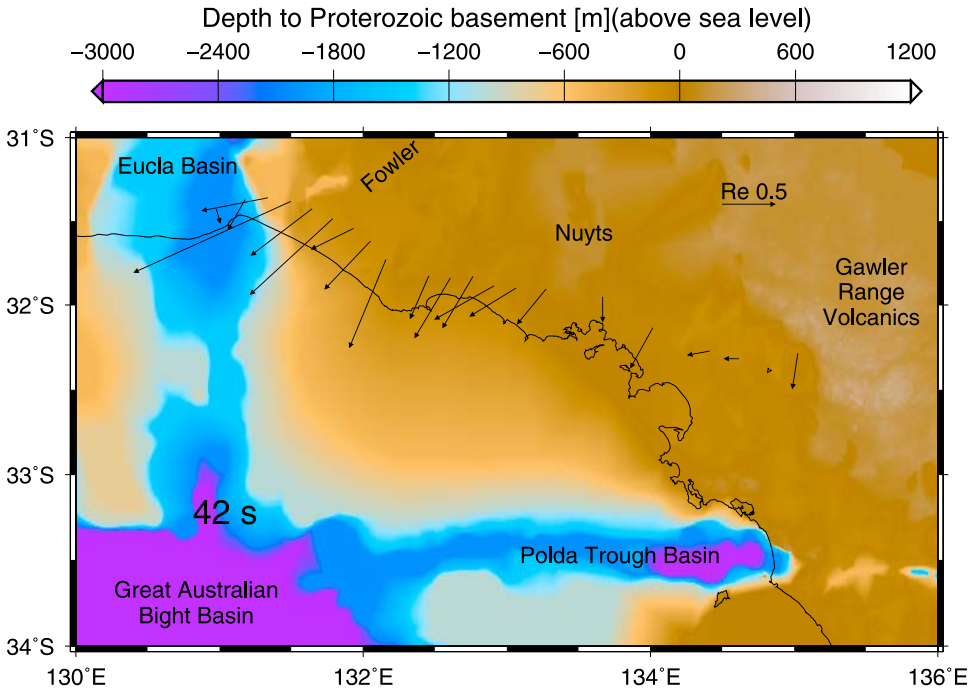

Figure 6. Real induction arrows at a period of 42 s superimposed on the Depth to Proterozoic basement map for the survey area and the continental slope. The basement maps indicate the thickness of the sedimentary basins throughout the area and exceed thicknesses of thousands of meters underneath the western part of the profile and to the south in the Polda Trough and the abyssal plains of the Great Australian Bight.

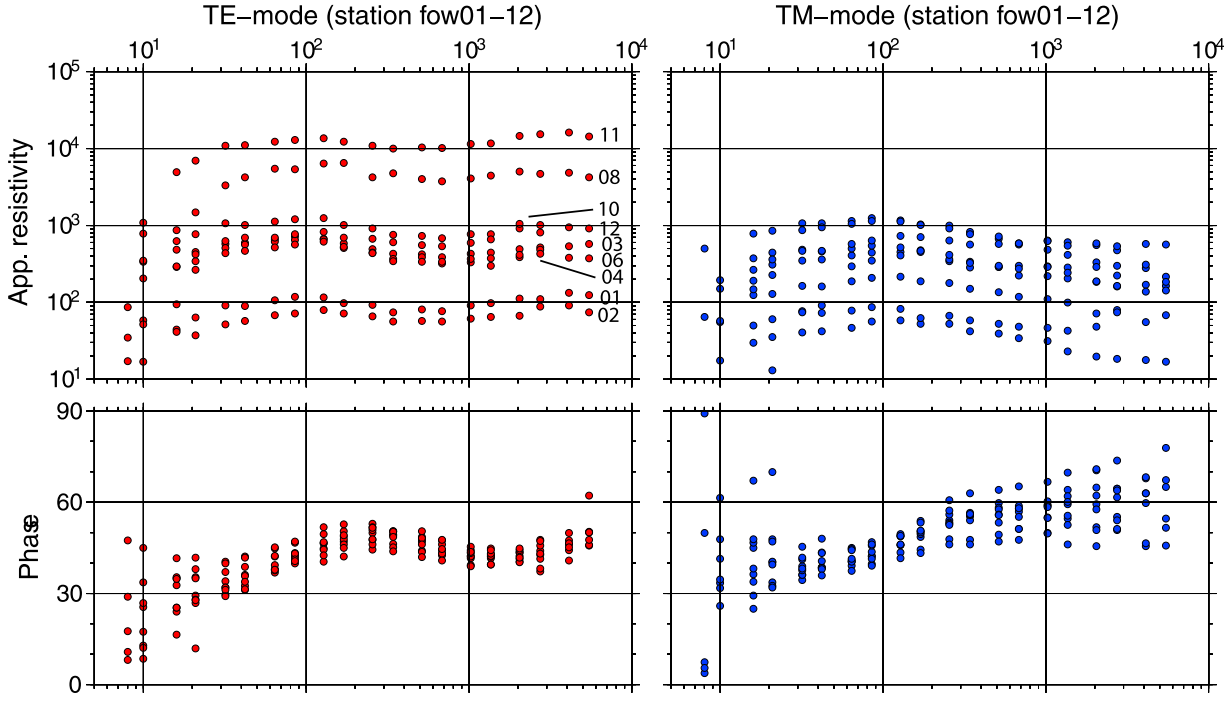

Figure 7. Apparent resistivities and phases for stations 01 to 12 of the eastern part of the profile. Numbers at the top left indicate stations corresponding to the apparent resistivity curves. The TE mode responses (E field north-south) show a much smaller variability in the phases than the TM mode, while the corresponding apparent resistivities vary by more than 2 orders of magnitude. The TE mode response is therefore more severely affected by static shift due to the charge accumulations along strong resistivity contrast between ocean and the resistive crust south of the profile line (cf. Figure 1).

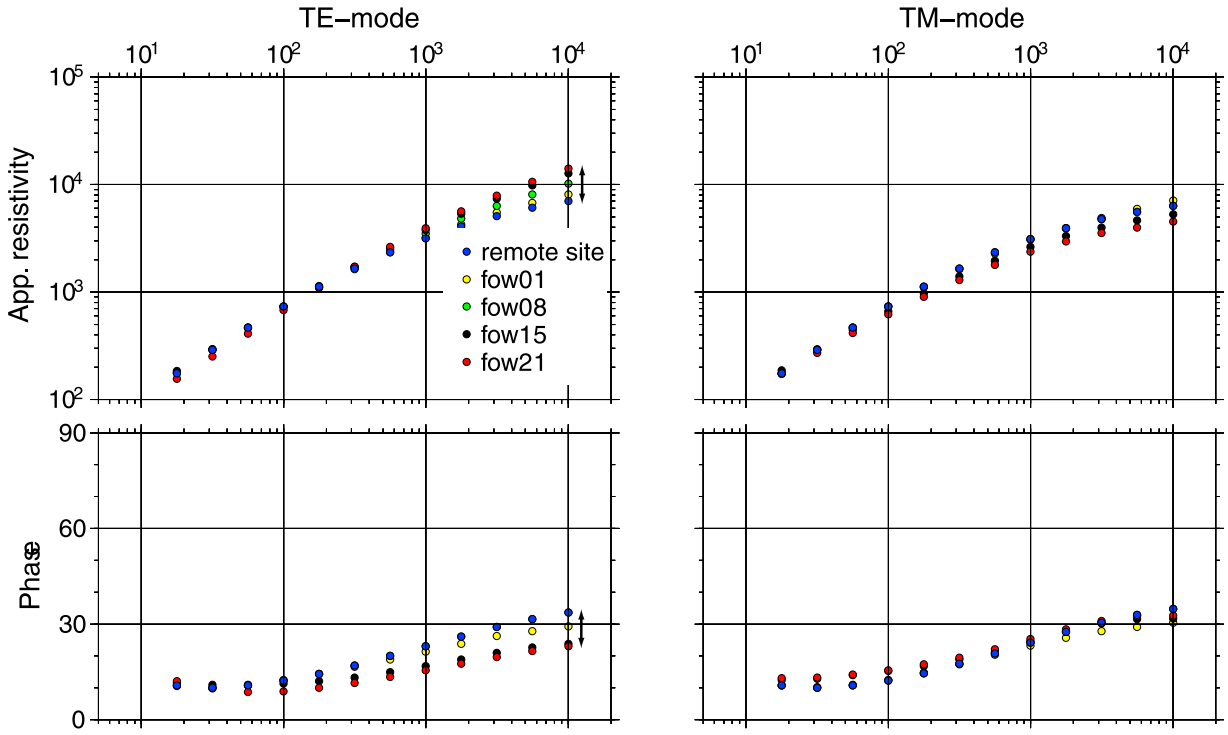

Figure 8. Apparent resistivities and phases for stations 01, 08, 15, and 21 compared to a remote site about 600 km inland computed from a two-layer model with resistivities of 50 Ωm m−1 in the top 5 km and 10,000 Ωm m−1 below. The ocean and sediments are also included in the forward model. The remote site (blue) indicates the undistorted two-layer response far away from the ocean. For long periods, the TE mode shows a slight downward bias of the TE phases and associated upward bias of apparent resistivities. The TM mode is not affected as strongly. This can result in overestimation of the resistivities at long periods in 2-D modeling.

sediments. The responses show that a 2-D inverse model could potentially exhibit too high resistivity values for deep structures.

5. Dimensionality and Electrical Strike

[22] For most periods the induction arrows are oriented at an oblique angle to the profile line, suggesting different strike directions due to shallow structures (ocean and sediments) and deeper crustal features. Therefore it is necessary to determine the dimensionality and electrical strike direction before a 2-D inversion is attempted. Here, we use the phase tensor approach [*Caldwell et al.*, 2004] and the phase-sensitive skew according to *Bahr* [1988] in order to firstly determine whether the stations fulfill assumptions for two-dimensionality throughout the recorded period range and secondly to find a common strike direction for which the two-dimensionality is optimized.

[23] In a strict 2-D scenario, the impedance tensor can be rotated to the line of strike resulting in vanishing diagonal components $Z_{x'x'} = Z_{y'y'} = 0$. Usually, the skew is a measure of the departure from that condition. *Bahr* [1988] introduced the phase-sensitive skew η, based on the condition that each column of the rotated impedance tensor (i.e., $Z_{x'x'}$ and $Z_{y'x'}$) has to have the same phase in a 2-D scenario. A departure from that condition results in skew values $\eta > 0$ and indicates three-dimensionality. Similarly, *Caldwell et al.* [2004] introduced the phase tensor $\mathbf{\Phi} = \Re(Z)^{-1}\Im(Z)$, which is symmetric in a geoelectrically 1-D or 2-D subsurface. The phase tensor skew is defined as

$$\beta = \frac{1}{2}\tan^{-1}\left(\frac{\Phi_{12} - \Phi_{21}}{\Phi_{11} + \Phi_{22}}\right), \tag{2}$$

and is nonvanishing in a regionally 3-D environment. If the three-dimensionality is only locally present, e.g., for length scales smaller than the skin-depth of the MT measurements, the phase tensor skew may be vanishing, however. Figure 9 illustrates the Bahr's and the phase tensor skew estimates for the entire profile. In general, $\eta < 0.3$ and $|\beta| < 5°$ are a soft condition for a quasi 2-D resistivity distribution, and visual inspection of the two skew pseudosections confirm that most periods between stations 01–14 on top of the GRV and the Nuyts Domain are 2-D. For the western part of the profile, stations 15–22, situated in the Fowler Domain, increasingly exhibit three-dimensionality for periods longer than a few hundred seconds. It is worth noting that the period range indicating a 3-D resistivity distribution increases from east to west for both skew definitions, i.e., between 500 and 5000 s underneath station 17 to a range of ≈100–5000 s underneath station 22. Tentatively, this suggests a superposition of influences of the north-south trending conductivity anomaly and sedimentary basin to the west and the conductive sediments/ocean water

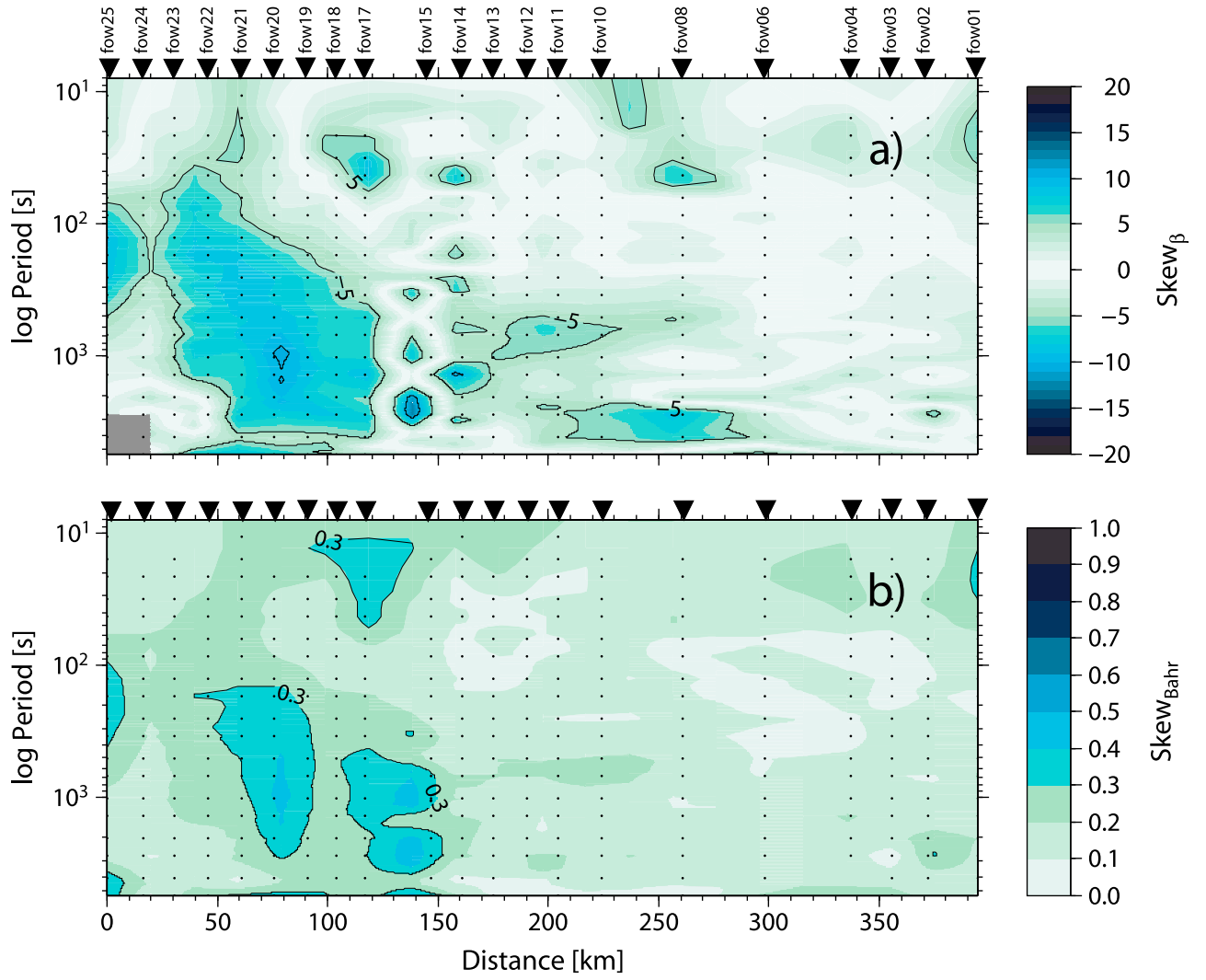

Figure 9. (top) Pseudosection of the skewness of the phase tensor [*Caldwell et al.*, 2004] and (bottom) the impedance tensor after Bahr's definition [*Bahr*, 1988]. Phase tensor skew $\beta < 5$ can be tentatively regarded as a quasi 2-D resistivity distribution, as well as skew's smaller than 0.3 in Bahr's definition. On the basis of this definition, the resistivity distribution is 2-D/3-D between 20 s and 200 s underneath stations 14–21 and is quasi 2-D for the other stations and periods.

to the south. The periods showing three-dimensionality are subsequently discarded during the 2-D inverse modeling.

[24] Orientation of phase tensor ellipses are approximately north-south, indicating major current flow perpendicular to the profile (Figure 4). Increasing ellipticity of the phase tensor ellipses with period suggest an increasing phase split between the xy and yx components of the impedance tensor. Minimum phase values are generally large for the eastern stations and decrease for stations overlying the Fowler Domain. This suggests that the underlying structure is more resistive across the Nuyts Domain and the GRV. Low minimum phase values of about 10° for the three western-most stations 23–25 suggest a more conductive shallow subsurface, which is in line with the findings of the forward modeling study shown above.

[25] Phase tensor ellipse orientations are parallel or perpendicular to the geoelectric strike in the case of a 2-D distribution. Here the ellipses are aligned with the strike of the fault zones (cf. Figure 1). The orientation of the ellipses have subsequently been used to determine a common geoelectric strike of the profile. Given that most of the stations and periods display 2-D behavior, the strike angle obtained can be utilized to rotate the data before the 2-D inversion. Figure 10 shows rose diagrams of the strike directions obtained from the phase tensor analysis by averaging over three period bands for all stations (Figure 10a) and period-averaged strike directions for all stations along the profile (Figure 10b). Figure 10a illustrates that the strike is more or less constant at 15° between 10 and 1000 s and rotates to north-south for longer periods. This strike coincides with the orientation of the main shear zones perpendicular to the profile (cf. Figure 1).

[26] Figure 10b shows that the spatial variability across the profile line lies within 0° and 30°. There is little variation within geological domains and most of the variability is between domains. Except for 13–15, all stations east of

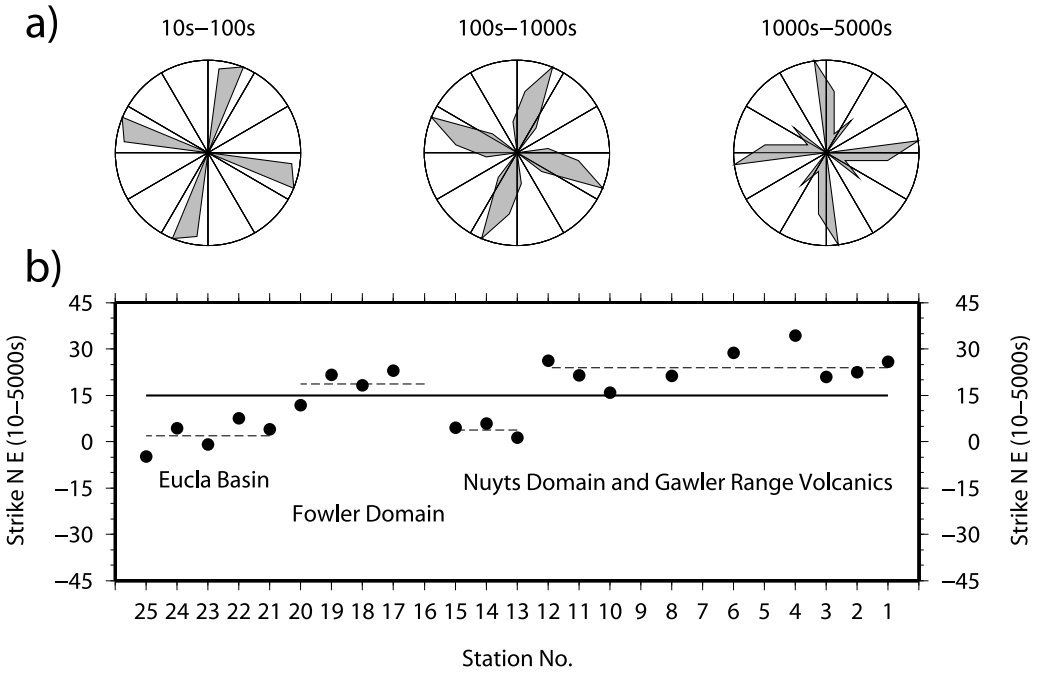

Figure 10. Geoelectric strike determination of the Fowler profile. (a) Rose diagrams depicting strike directions of all stations for three period bands (10–100 s, 100–1000 s, and 1000–5000 s), indicating a small (max 20°) variation in strike over period. (b) Period-averaged strike directions over the entire profile indicate a common strike of N15°E (solid line). Dashed lines show the average geoelectric strike directions within adjacent domains.

the Tallacootra Shear Zone, at the western margin of the Fowler Domain, have an average strike of approximately 15–20°. In the Eucla Basin, the strike direction deflects to 0°N for the westernmost stations.

[27] Given these findings, the rotated impedance tensor coordinate system $\{x', y'\}$ now has x' aligned with N15°E and we assign the $x'y'$ component of the impedance tensor to the TE mode (transverse electric) and the $y'x'$ component to the TM mode (transverse magnetic). Therefore the x' component of the rotated coordinate system is approximately parallel to the known geological domain boundaries and the shear zones visible in the potential field data (cf. Figures 1 and 2).

6. Two-Dimensional Resistivity Model

[28] Following the arguments above, the data has been subsequently rotated to N15°E. Periods exhibiting 3-D effects for stations toward the western end of the profile have been excluded and are not used in the 2-D inverse modeling. The rotated off-diagonal elements of the impedance tensor ($Z_{x'y'}$ and $Z_{y'x'}$) and the profile-parallel geomagnetic transfer function responses $\boldsymbol{T}$ were inverted in a 2-D sense for the period range between 10 s and 5000 s on a 315 × 46 rectangular grid using the 2-D inversion code of *Rodi and Mackie* [2001]. Owing to the fact that the TE mode exhibits large static shifts, the errors on the TE mode apparent resistivities ρ_a are set to 100%, while giving a higher weight to the TE phases with an error floor of 1° as they are not affected by static shift. The tipper data is consistent across the profile line and the error floor was set to 0.02. Initially, the inversion is started off with fitting only the TE mode and the tipper until the model converges. Subsequently, the TM mode information is added to the inverse process. Here, the error floors on the apparent resistivity and phases are 10% and 1°, respectively, and are therefore weighted higher than the TE mode. Upon convergence of the TE mode, TM mode, and the tipper, the inversion is allowed to freely adjust static shift in the TE mode regardless of the high error bars in the apparent resistivities. In general, this has improved the root mean square (rms) misfit, e.g., in our final model from 1.86 to 1.56. The misfits for selected stations are shown in Figure 3 and pseudosections of the TE mode, TM mode, and the tipper in Figure 13.

[29] Achieving a reliable model from a nonlinear and regularized inversion procedure requires careful tests of inversion parameters. These measures ensure not to get trapped in local minima during the inversion and to be confident the main features of the model are robust to varying parameters. The inversion minimizes a regularized penalty functional $\varphi = \varphi_d + \tau L(\log(\rho) - \log(\rho_0))$, where the tradeoff parameter τ balances the influence of the data misfit functional φ_d and the structure penalty term $L(\log(\rho) - \log(\rho_0))$. L is a simple second-difference operator of the model, while the a priori model is defined through the ρ_0 term. In order to obtain a final model with a good RMS misfit, we have tested various starting models with different resistivities. The Eucla Basin at the western end of the profile has also been included by assigning a resistivity of $\rho = 20$ Ωm m−1 to the corresponding cells. Subsequently, the inverse pro-

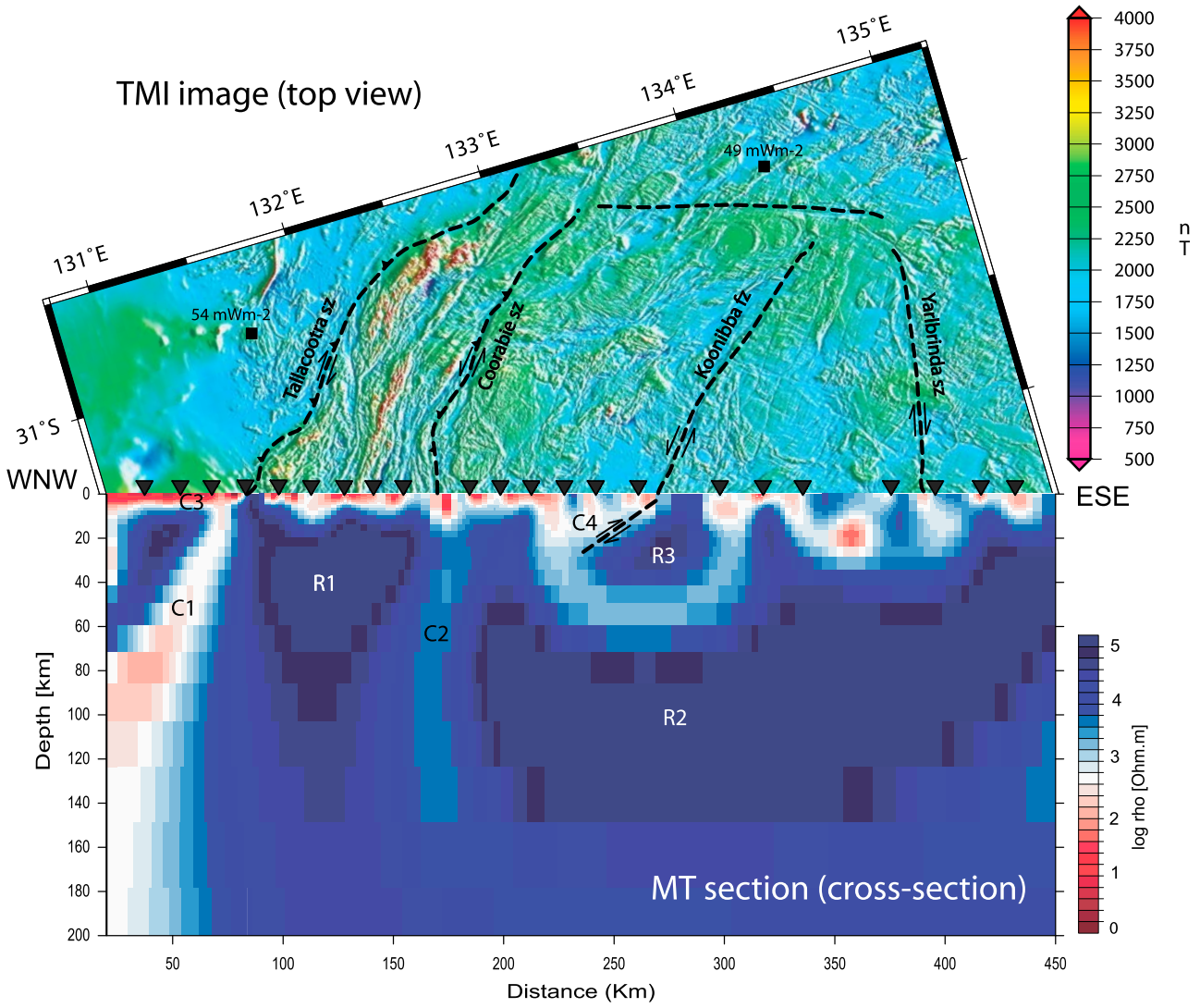

Figure 11. (bottom) Resistivity model (cross section) obtained from 2-D inversion compared to (top) TMI image (plan view). Black triangles denote MT station locations along the profile line at the fold line between the Mt cross section and the TMI image. Major shear zones have been retraced in the TMI image (dashed black lines). Tallacootra, Coorabie shear zones, and the Koonibba fault zone have an electrical expression at depth. The Yarlbrinda shear zone to the east does not show a distinct crustal expression in the resistivity image. Heat flow data (black squares) based on *Hand et al.* [2007].

cess was set to solve away from the a priori model with sedimentary basins included. The tradeoff parameter τ has been tested between values of 1000 and 1, and a final value of 10 was chosen using the L curve criteria applied to a RMS misfit versus model roughness plot [*Aster et al.*, 2005]. The result is a model that fits the data without adding spurious structure, which does not improve the overall misfit considerably.

[30] The final resistivity model in Figure 11 has been obtained from a 100 Ωm m−1 half-space including the sedimentary basins with a resistivity of 20 Ωm m−1. It should be noted that this model is very similar to other models obtained from different starting half-spaces; hence the features discussed here are robust in the sense that they are relatively insensitive to changes in the inversion parameters. In general, the resistivity structure of the lower crust and upper mantle is very resistive with cell values exceeding 10^5 Ωm m−1. A very resistive nucleus, labeled R1 in Figure 11 extends between depths of 20 km and 120 km underneath the Fowler Domain. Similarly, high resistivities are found in the lower crust and upper mantle underneath the Nuyts Domain and the GRV to the east, labeled R2 in Figure 11. The feature R2 extends from depths of ~40 km to 160 km. The high resistivity values have to be treated with caution as the conductive ocean to the south can have some inductive effect on the TE responses as shown in section 4, which results in too high resistivity values. Preliminary 3-D inverse modeling of the 2-D line incorporating the ocean as a priori information reveals lower resistivities for the Archaean crust than obtained here, further suggesting that the resistivity values obtained from 2-D modeling are slightly higher [*Thiel*, 2008]. How-

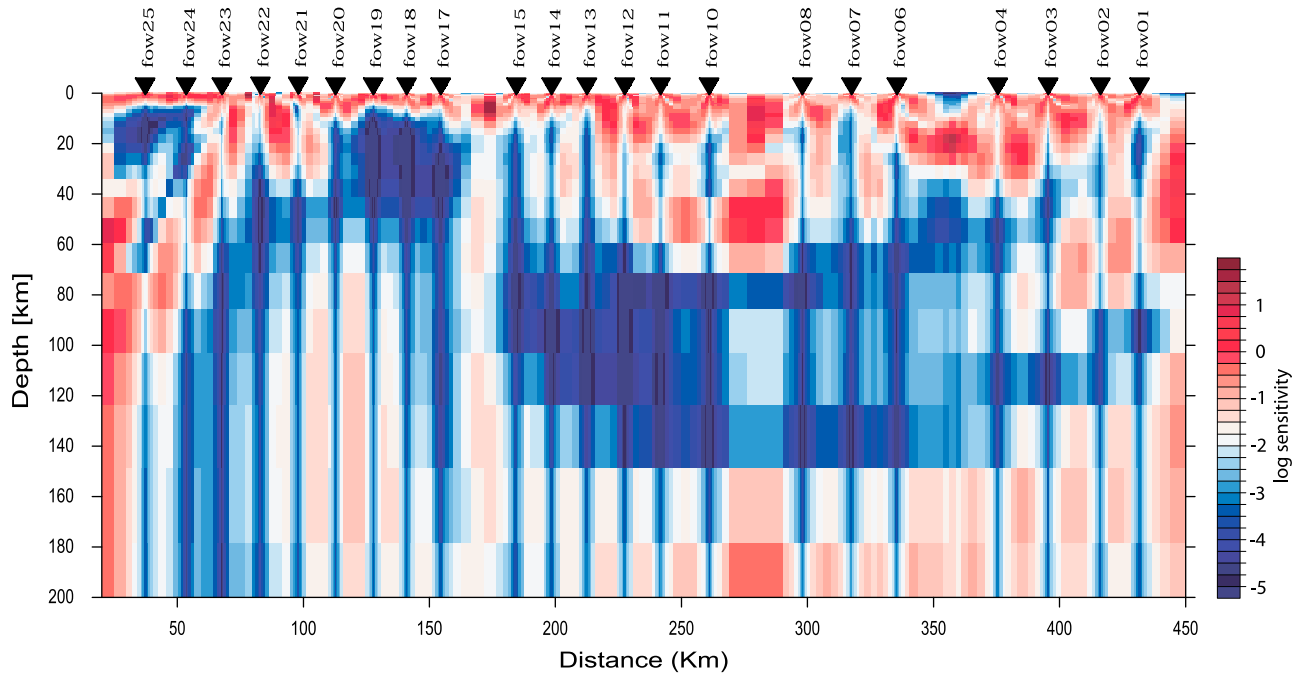

Figure 12. Sensitivity map of the Fowler profile, showing a correlation between zones of low resistivity/high sensitivity and high resistivity/low sensitivity, respectively (cf. Figure 11).

ever, similarly high resistivity values have been reported in the Slave Craton [*Spratt et al.*, 2009]. The two highly resistive zones are separated by a near-vertical feature of 1000 Ωm m−1 resistivity, labeled C2. Near the surface, feature C2 corresponds to the outcrop location of the Coorabie Shear Zone and increases in conductivity by 1–2 orders of magnitude for depths shallower than 15 km. Another subvertical conductive feature C1 is situated to the west of the resistive nucleus R1 underneath the Fowler Domain. Its resistivity is higher than C2 at around 100 Ωm m−1. It represents a major feature of the crust and upper mantle and its eastern margin marks a distinct resistivity interface from the surface to depths of more than 100 km and corresponds to surface expressions of the Tallacootra shear zone [*Fraser and Lyons*, 2006]. The conductive sedimentary Eucla basin dominates the top few kilometers underneath stations 23–25 (labeled C3 in Figure 11) and exhibits resistivities of around 10 Ωm m−1; note that this feature has been included as a priori information in the inversion process. In the vicinity of the Koonibba fault zone in the central part of the profile a resistivity interface to depths of about 40 km separates a thicker conductive (several hundreds Ωm m−1) feature C4 from a shallow (0–40 km depth) resistor with about 10,000 Ωm m−1. The resistivity contrast corresponds to the Koonibba fault zone at the surface but dips at a shallower angle than C1 and C2 at about 45°.

[31] The model described here is robust to variations in inversion parameters; however, the final model obtained in Figure 11 was further scrutinized with sensitivity tests to ensure robustness. Figures 12 and 13 illustrates a sensitivity map of the resistivity profile, obtained from visualization of the diagonal part of $A^T R_{dd}^{-1} A$, with A the sensitivity matrix and R_{dd}^{-1} the inverse of the data covariance matrix. T denotes the transpose of a matrix. Figure 12 shows that zones of low sensitivity correspond to zones of high resistivity in the model (Figure 11), demonstrating that the highly resistive areas in the model are not very sensitive to changes, i.e., perturbations of cells will not cause a great change in overall RMS misfit of the model. However, the high resistivity zone R3 in Figure 11 has a much higher sensitivity, implying that this feature cannot be perturbed with causing a substantial change in misfit. Indeed, replacing R3 with varying resistivities and computing the misfits by forward modeling reveals that this feature is very sensitive to changes in resistivities of the corresponding cells. The conductors C1 and C2 also exhibit increased sensitivity to changes according to Figure 12. Naturally, the same can be said about the conductive cover across the entire profile, which is due to the proximity to the measurement sites and thus strength of the inducing field.

[32] In addition to visual inspection of the sensitivity matrix, a series of forward modeling tests on the conductors C1 and C2 were performed. Feature C1 has been replaced by a 60 km wide 10,000 Ωm m−1 resistor between depths of 35 km and 100 km, which has increased the RMS misfit to an unacceptable 2.71 as compared to the original RMS of 1.56. The conductor reappeared after inverting the model with the resistor and the model reverted back to an RMS of 1.57. Keeping the resistor fixed at 10,000 Ωm m−1 during the inversions does not achieve a similar misfit (1.67) and the inversion algorithm increases the conductivity above 35 km and below 100 km instead of compensating for the resistor. Subsequently, an a priori inversion was tried with the resistor included as a "soft" constraint on the inversion, similar to tests undertaken by *Becken et al.* [2008]. Even though the inversion tries to find a model around the prior model with the resistor between 35 km and 100 km depths, the final model forces a subvertical con-

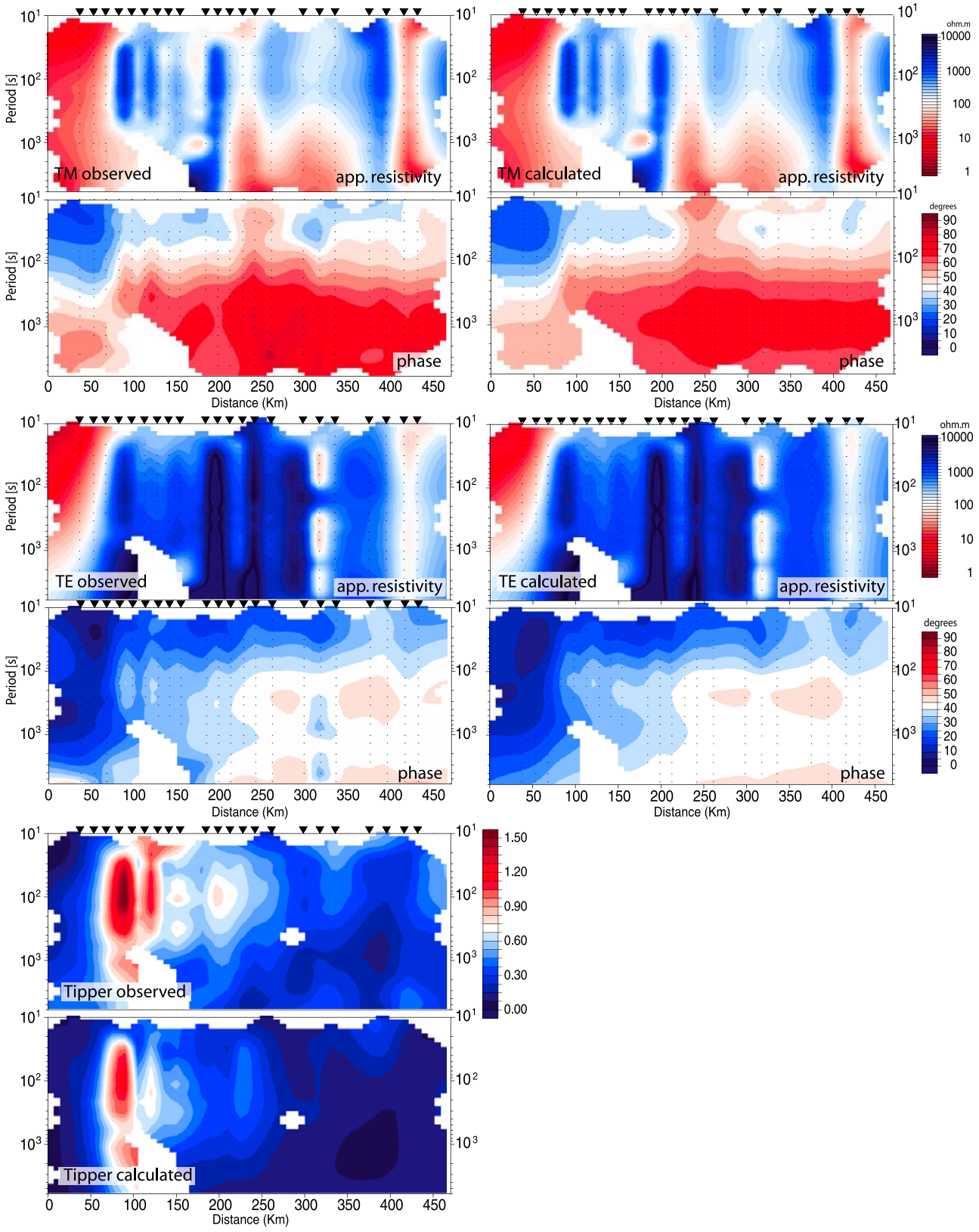

Figure 13. Pseudosection of the TE mode, TM mode, and tipper magnitude of the observed data and calculated 2-D model response as a function of period. Apparent resistivities and phases are chosen to display the TE and TM mode.

ductor from top to bottom of the resistor. The depth extent of C1 was also tested and forward modeling shows that depths in excess of 200 km are required by the model to achieve similar RMS misfits as the model in Figure 11. Similarly, the conductor C2 has been replaced by a resistor of 10,000 Ωm m−1 resistivity, connecting the lower crust and upper mantle resistors R1 and R2 in Figure 11. Upon inclusion, the RMS misfit increased to 2.1 and inversions from the altered model resulted again in reappearance of the conductor C2 and an RMS misfit of 1.59. The question remains whether the conductor C2 needs to be as wide as postulated by the inverse model in Figure 11 or if it can be more narrow with lower resistivity values. The conductor C2 does not lie directly underneath a MT station and the resolution is therefore limited compared to other features in the model. The width of C2 was tested by including a vertical and narrow structure of 100 Ωm m−1 replacing the subvertical wider conductor C2 of resistivities higher than 1000 Ωm m−1. The 100 Ωm m−1 replacement was subsequently locked during the inverse process. The model has a final RMS of 1.7, as compared to 1.57 for the model shown in Figure 11. Further tests without locking the narrow conductor resulted in a wider conductor similar to C2 in Figure 11. Given the current inversion parameters and resolution of the model it is hard to resolve the actual width and resistivity of the conductor, but the tests indicate a rather high resistivity of above 1000 Ωm m−1. The dip angle of the features C1 and C2 has also been varied to estimate the possible dip angles on the shear zones. Inversion of the varying dip angles ended in very similar angles obtained in the model, e.g., a slight westward dip for feature C1 and near vertical for feature C2.

[33] At last, the depth of the resistors R1 and R2 proved to be well constrained by the model. Changes resulted in unacceptable RMS misfits, which is supported by visualization of the sensitivity matrix in Figure 12, where the sensitivities increase for depths larger than the bottom of resistors R1 and R2.

7. Discussion

[34] The resistivity profile is dominated by very resistive lower crust and upper mantle material exceeding resistivities of 10,000 Ωm m−1. Olivine is the dominant mineral between the bottom of the crust and the 410 km discontinuity [*Nover*, 2005]. The very high resistivity for the lower crust and upper mantle underneath the profile suggest a thick cratonic keel underneath the Nuyts and Fowler Domain. Laboratory measurements on dry olivine between temperatures of 800°C and 1000°C exhibit resistivities similar to observations in this study (features R1 and R2 in Figure 11) [*Wang et al.*, 2006]. Olivine also shows anisotropy in conductivity depending on the crystallographic directions [*Schock et al.*, 1989; *Wannamaker and Duba*, 1993; *Du Frane et al.*, 2005]. Increased conductivity by a factor of 2 can be observed in the crystallographic [001] direction of olivine. An alignment of olivine can occur through mantle flow or potentially plate motion. *Simpson* [2001] inferred a N38°E strike in the upper mantle of Central Australia, deviating from the N9.6°E orientation of the present Australian plate motion and thus suggesting a resistance to mantle flow. If the general strike direction is also applicable to South Australia it would be approximately perpendicular to the line of profile in Figure 11 and the olivine imaged with the TE mode of the MT response (currents aligned roughly north-south) would correspond to the more resistive crystallographic [100] direction. This further supports the high resistivities seen in this study for upper mantle depths. The depth of the lithosphere is at around 160 km underneath the Nuyts Domain and appears to shallow to about 100 km to 120 km underneath the Fowler Domain.

[35] Images of isotropic shear wave speed models from tomographic inversions show a boundary at 75 km to 100 km depth across the eastern side of the Nuyts Domain [*van der Hilst et al.*, 1998; *Kennett et al.*, 2004; *Fishwick et al.*, 2005; *Fishwick and Reading*, 2008] with fast shear wave velocity to the west underneath the western Nuyts Domain and the Fowler Domain. Slower shear wave speeds are observed underneath the eastern Nuyts Domain and the Gawler Range Volcanics. The MT model shows large-scale lateral changes rather at shallower depths than 75 km, the crust underneath the Nuyts Domain is more conductive (several hundred Ωms per meter) compared to the very resistive crust underneath the Fowler Domain at similar depths. The shear wave speed models do not show crustal perturbations underneath the Coorabie and Tallacootra shear zones. Grain size variations have an effect on the shear wave speeds and have been discussed for depths greater than 200 km [*Faul and Jackson*, 2005], but in this case it is not clear whether grain-size variations across relatively narrow shear zones has an effect on the seismic tomographic inversion images. For depths of about 150 km the shear wave speeds do not show great variations, but seem to show a reversal in wave speed perturbations at depths greater than 200 km, i.e., higher wave speeds to the east (cf. Figure 3 in the work of *Fishwick and Reading* [2008]). The seismic wave speed is primarily dependent on temperature and high wave speeds relate to cold Archaean lithospheric roots. The MT model begins to lose resolution at depths greater than 200 km but there is a correlation to the MT model in that the cratonic root appears to extend deeper underneath the Nuyts Domain than underneath the Fowler Domain.

[36] It is interesting to note that the top of the cratonic lithosphere R1 is closer to the surface compared to R2. *Thomas et al.* [2008] report the highest estimated pressure-temperature (P-T) conditions of mafic granulites in the Fowler Domain reach ~8–9.5kbar and 780–860°C corresponding to depths of ~30 km. The metasediments in the Fowler Domain are of higher metamorphic grade compared to rocks in the Nuyts Domain and have been exhumed from greater depths. This notion seems to be reflected in the resistivity profile, where the horizontal boundary between the more conductive upper crust and the resistive cratonic root is deeper underneath the Nuyts Domain at depths of around 40 km compared to only about 20 km underneath the Fowler Domain.

[37] The Tallacootra shear zone [*Teasdale*, 1997; *Fraser and Lyons*, 2006] is imaged as a steep-dipping conductor (C1 in Figure 11) with resistivities of several hundred Ωms per meter. Outcrops show subvertical mylonitic fabrics with age data suggesting most recent activity around 1450 Ma in a transpressional regime as constrained from $^{40}Ar/^{39}Ar$

data [*Fraser and Lyons*, 2006]. The mylonitic fabrics point toward intense shearing during the active phase of the Tallacootra shear zone. Partial melts do not seem to be an option for enhancing the conductivity; the only two heat flow measurements remotely near the Tallacootra shear zone indicate values of 54 mW m-2 to the northwest of the shear zone and 46 mW m-2 just north of the Nuyts Domain (cf. Figure 11). Even though heat flow measurement locations are very sparsely populated, there is no reason why there should be anomalously high heat flow associated with the Tallacootra shear zone. Several other agents, such as fluids and sulphide/graphite mineralization are frequently proposed for enhancing conductivity associated within shear zones [*Wannamaker et al.*, 2002; *Pous et al.*, 2004; *Ritter et al.*, 2005]. Given the depth extent of the enhanced conductivity of C1, fluids can be ruled out since they cannot be trapped over such an extended period of time, especially in stable regimes such as here. Metallic films of graphite/sulphide along intensely sheared faults and in fold hinges associated with the transpressional setting of the Tallacootra shear zone would be an agent that cannot be dismissed [*Ritter et al.*, 2003; *Thiel et al.*, 2005]. However, the relatively high resistivity of the shear zone C1 suggest that the mineral phase is not very well connected, otherwise an increase in conductivity by several orders of magnitude would have to be observed. *ten Grotenhuis et al.* [2004] have reported on increases in conductivity by 1 to 2 orders of magnitude for fine-grained (1–5 μm) polycrystalline forsterite, a Mg end-member of olivine, in shear zones in the upper mantle. The mylonitic nature of the Tallacootra shear zone suggests that enhanced conductivity caused by grain boundary diffusion seems a viable idea in view of the conductivity contrast between the resistive keel R1 underneath the Fowler Domain and the crustal and upper mantle conductor C1.

[38] A similar argument applies to the conductor C2 in the lower crust and upper mantle, which spatially correlates with the Coorabie shear zone at the surface. Its resistivity is about 2–5 times lower than C1 but still about two orders of magnitude higher than the adjacent and resistive lithospheric blocks R1 and R2. Limited outcrops of the Coorabie shear zone show mylonitic fabrics formed at upper greenshist to lower amphibolite-facies conditions. Similar to the Tallacootra shear zone, the mylonitic fabrics are steep and strike-slip coupled with dip-slip movement has been present [*Teasdale*, 1997; *McLean and Betts*, 2003; *Thomas et al.*, 2008]. The even lower conductivity of this shear zone C2 compared to C1 favors enhanced conductivity due to an increase in grain boundary diffusion in fine-grained shear zones [*ten Grotenhuis et al.*, 2004].

[39] Forward modeling studies of potential field data across the Coorabie shear zone indicate northwest dipping interfaces [*Thomas et al.*, 2008]. The dip angle is very steep at around 80° and matches the findings from the resistivity model. However, the depth constraint of the potential field data modeling is restricted to 15 km depth. There are no forward modeling studies across the Tallacootra shear zone, but interpretations of TMI suggests a northwest dip similar to the Coorabie shear zone [*Thomas et al.*, 2008].

[40] The upper and middle crust underneath the Nuyts Domain is dominated by a resistivity interface between a more conductive region C4 and a near-surface resistor R3. The interface dips at an angle of ~45° to the west and coincides with the Koonibba fault zone near the surface. To the west of the Koonibba fault zone outcrops show intrusion of the Mesoproterozoic Munjeela Suite granites. *Payne* [2008] provides evidence of crystallization at more than 20 km depth for the Munjeela granites during the period ~1625–1590 Ma from P-T constraints on metamorphism of the metasedimentary enclaves (7kbar, 650°C). The different P-T conditions of rocks on both sides of the Koonibba fault zone, the Munjeela granites and the St. Peter Suite in the west and east, respectively, are represented by electrically different responses on both sides of the fault zone, with the Munjeela Suite having a lower resistivity of several hundred Ωms per meter.

[41] The Yarlbrinda shear zone crosses the profile just west of station 03 and does not have a distinct electrical response as the other framework shear zones along the profile. The TMI image also does not show a strong expression and other events appear to have overprinted the shear zone (cf. Figure 11).

8. Conclusions

[42] A magnetotelluric survey was collected across the western margin of the late Archaean-early Proterozoic Gawler Craton extending from the Gawler Range Volcanics in the east over the Nuyts Domain and the interpreted mobile belt of the Fowler Domain into the Eucla Basin in the west. The data provide information about the resistivity structure of the crust and upper mantle beneath an east-west profile. Phase tensor analysis indicate predominantly two-dimensional behavior with a geoelectric strike of N15°E. The strike direction coincides with strike directions of major domain boundaries and shear zones inferred from potential field data and limited outcrop information. Three-dimensionality in the data can be explained through a superposition of ocean effect and sedimentary basins to the south of the profile and enhanced conductivity beneath the profile. Two-dimensional inverse modeling of a suitable subset of the data reveals resistivity features corresponding to major geological domains and features present in potential field maps.

[43] The lower crust and upper mantle shows generally very high resistivities representing dry olivine. Two subvertical zones of enhanced conductivity extend from the crust into the upper mantle and are believed to correspond to mylonitic shear fabric and fine-grained olivine. These zones spatially correspond to outcrops of the Tallacootra and Coorabie shear zone at the surface. The Koonibba fault zone is imaged as a west-dipping resistivity interface between more conductive material to the west corresponding to the Munjeela granite and the more resistive material of the Nuyts Domain to the east.

[44] An interesting feature is the high resistivity of the lithosphere beneath the interpreted mobile belt of the Fowler Domain. MT studies usually indicate at least moderate enhancement in conductivity associated with mobile belts worldwide [*Ritter et al.*, 2003; *Ferguson et al.*, 2005]. However, this study shows a different electrical response, suggesting that the lithosphere underneath the Fowler

Domain may be related to the resistive cratonic lithosphere of the Archaean Gawler Craton imaged beneath the Nuyts Domain.

[45] **Acknowledgments.** Funding for this project was provided by ARC Linkage Project LP0454301, Developing a tectonic framework for the Gawler Craton: Paving the way for successful mineral exploration programs. Department of Primary Industries and Resources South Australia provided logistical support. Martin Hand provided very valuable information on the regional geology of the area. Ian Ferguson and an anonymous reviewer are thanked for their valuable comments and helped to improve the manuscript. Magdalena Nenycz-Thiel is thanked for assistance in the field. Most of the images were generated with the GMT package of *Wessel and Smith* [1998]. ST's contribution forms TRaX Record 60.

References

Aster, R., B. Borchers, and C. Thurber (2005), *Parameter Estimation and Inverse Problems (International Geophysics)*, Elsevier, Burlington, Mass.

Bahr, K. (1988), Interpretation of the magnetotelluric impe dance tensor: regional induction and local telluric distortion, *J. Geophys.*, *62*, 119–127.

Becken, M., O. Ritter, S. K. Park, P. A. Bedrosian, U. Weckmann, and M. Weber (2008), A deep crustal fluid channel into the San Andreas Fault system near Parkfield, California, *Geophys. J. Int.*, *173*(2), 718–732.

Betts, P. G., D. Giles, G. S. Lister, and L. R. Frick (2002), Evolution of the Australian lithosphere, *Aust. J. Earth Sci.*, *49*, 661–661.

Cagniard, L. (1953), Basic theory of the magneto-telluric method of geophysical prospecting, *Geophysics*, *18*, 605–635.

Caldwell, T. G., H. M. Bibby, and C. Brown (2004), The magnetotelluric phase tensor, *Geophys. J. Int.*, *158*, 457–457.

Chave, A., and D. Thomson (1989), Some comments on magnetotelluric response function estimation, *J. Geophys. Res.*, *94*, 14,215–14,225.

Chave, A., D. Thomson, and M. Ander (1987), On the robust estimation of power spectra, coherences, and transfer functions, *J. Geophys. Res.*, *92*, 633–648.

Daly, S., C. Fanning, and M. Fairclough (1998), Tectonic evolution and exploration potential of the Gawler Craton, South Australia, *J. Aust. Geol. Geophys.*, *17*, 145–168.

Direen, N., A. Cadd, P. Lyons, and J. Teasdale (2005), Architecture of Proterozoic shear zones in the Christie Domain, western Gawler Craton, Australia: Geophysical appraisal of a poorly exposed orogenic terrane, *Precambrian Res.*, *142*, 28–44.

Du Frane, W. L., J. J. Roberts, D. A. Toffelmier, and J. A. Tyburczy (2005), Anisotropy of electrical conductivity in dry olivine, *Geophys. Res. Lett.*, *32*, L24315, doi:10.1029/2005GL023879.

Evans, S., A. Jones, J. Spratt, and J. Katsube (2005), Central Baffin electromagnetic experiment (CBEX): Mapping the North American Central Plains (NACP) conductivity anomaly in the Canadian arctic, *Phys. Earth Planet. Inter.*, *150*, 107–122.

Fanning, C., A. Reid, and G. Teale (2007), A geochronological framework for the Gawler Craton, South Australia, *S. Aust. Geol. Surv. Bull.*, *55*, 258.

Faul, U., and I. Jackson (2005), The seismological signature of temperature and grain size variations in the upper mantle, *Earth Planet. Sci. Lett.*, *234*, 119–134.

Ferguson, I., et al. (2005), Geoelectric response of Archean lithosphere in the western Superior Province, central Canada, *Phys. Earth Planet. Inter.*, *150*, 123–143.

Fishwick, S., and A. Reading (2008), Anomalous lithosphere beneath the Proterozoic of western and central Australia: A record of continental collision and intraplate deformation?, *Precambrian Res.*, *166*(1–4), 111–121.

Fishwick, S., B. Kennett, and A. Reading (2005), Contrasts in lithospheric structure within the Australian craton-insights from surface wave tomography, *Earth Planet. Sci. Lett.*, *231*(3–4), 163–176.

Flint, R., L. Rankin, and C. Fanning (1990), Definition - the Palaeoproterozoic St. Peter Suite of the western Gawler Craton, *Q. Geol. Notes Geol. Surv. S. Aust.*, *114*, 2–8.

Fraser, G., and P. Lyons (2006), Timing of Mesoproterozoic tectonic activity in the northwestern Gawler Craton constrained by 40Ar/39Ar geochronology, *Precambrian Res.*, *151*, 160–184.

Gamble, T., W. Goubau, and J. Clarke (1979), Magnetotellurics with a remote magnetic reference, *Geophysics*, *44*, 53–68.

Hamilton, M. P., A. G. Jones, R. L. Evans, S. Evans, C. Fourie, X. Garcia, A. Mountford, and J. E. Spratt (2006), Electrical anisotropy of South African lithosphere compared with seismic anisotropy from shear-wave splitting analyses, *Phys. Earth Planet. Inter.*, *158*, 226–239.

Hand, M., A. Reid, and L. Jagodzinski (2007), Tectonic framework and evolution of the gawler craton, southern australia, *Econ. Geol.*, *102*(8), 1377–1395.

Harinarayana, T., K. Naganjaneyulu, and B. Patro (2006), Detection of a collision zone in south Indian shield region from magnetotelluric studies, *Gondwana Res.*, *10*, 48–56.

Heinson, G., N. Direen, and R. Gill (2006), Magnetotelluric evidence for a deep-crustal mineralizing system beneath the Olympic Dam iron oxide copper-gold deposit, southern Australia, *Geology*, *34*, 573–576.

Hitzman, M., N. Oreskes, and M. Einaudi (1992), Geological characteristics and tectonic setting of Proterozoic iron oxide (Cu-U-Au-REE) deposits, *Precambrian Res.*, *58*, 241–287.

Jones, A. (1988), Static shift of magnetotelluric data and its removal in a sedimentary basin environment, *Geophysics*, *53*, 967–978.

Jones, A., I. Ferguson, A. Chave, R. L. Evans, and G. McNeice (2001), Electric lithosphere of the Slave craton, *Geology*, *29*, 423–426.

Kennett, B. L. N., S. Fishwick, A. M. Reading, and N. Rawlinson (2004), Contrasts in mantle structure beneath Australia: Relation to Tasman Lines?, *Aust. J. Earth Sci.*, *51*, 563–569.

Mackie, R. L., T. Madden, and P. Wannamaker (1993), Three-dimensional magnetotelluric modeling using difference equations—Theory and comparisons to integral equation solutions, *Geophysics*, *58*, 215–226.

McLean, M. A., and P. G. Betts (2003), Geophysical constraints of shear zones and geometry of the hiltaba suite granites in the western gawler craton, australia, *Aust. J. Earth Sci.*, *50*(4), 525–541.

Nover, G. (2005), Electrical properties of crustal and mantle rocks: A review of laboratory measurements and their explanation, *Surv. Geophys.*, *26*, 593–651.

Parker, A. (1993), Geological framework, in *The Geology of South Australia*, vol. 1, *The Precambrian*, edited by J. Drexel, W. Preiss, and A. Parker, page numbers?, Geol. Surv. of S. Aust., location?.

Payne, J. (2008), Palaeo- to Mesoproterozoic evolution of the Gawler Craton, Australia: Geochronological, geochemical and isotopic constraint, Ph.D. thesis, School of Earth and Environ. Sci., Univ. of Adelaide, Adelaide, SA, Australia.

Payne, J., K. Barovich, and M. Hand (2006), Provenance of metasedimentary rocks in the northern Gawler Craton, Australia: Implications for Palaeoproterozoic reconstructions, *Precambrian Res.*, *148*(3–4), 275–291.

Pous, J., G. Munoz, W. Heise, J. Melgarejo, and C. Quesada (2004), Electromagnetic imaging of Variscan crustal structures in SW Iberia: The role of interconnected graphite, *Earth Planet. Sci. Lett.*, *217*, 435–450.

Ritter, O., U. Weckmann, T. Vietor, and V. Haak (2003), A magnetotelluric study of the Damara Belt in Namibia: 1. Regional scale conductivity anomalies, *Phys. Earth Planet. Inter.*, *138*, 71–90.

Ritter, O., A. Hoffmann-Rothe, P. A. Bedrosian, U. Weckmann, and V. Haak (2005), Electrical conductivity images of active and fossil fault zones, *Geol. Soc. London Spec. Publ.*, *245*(1), 165–186.

Rodi, W., and R. L. Mackie (2001), Nonlinear conjugate gradients algorithm for 2-D magnetotelluric inversion, *Geophysics*, *66*, 174–187.

Schock, R., A. Duba, and T. Shankland (1989), Electrical-Conduction in olivine, *J. Geophys. Res.*, *94*(B5), 5829–5839.

Simpson, F. (2001), Resistance to mantle flow inferred from the electromagnetic strike of the Australian upper mantle, *Nature*, *412*, 632–635.

Simpson, F., and K. Bahr (2005), *Practical Magnetotellurics*, Cambridge Univ. Press, New York.

Smith, W., and D. Sandwell (1997), Global sea floor topography from satellite altimetry and ship depth soundings, *Science*, *277*(5334), 1956–1962.

Spratt, J. E., A. G. Jones, V. A. Jackson, L. Collins, and A. Avdeeva (2009), Lithospheric geometry of the Wopmay orogen from a Slave craton to Bear Province magnetotelluric transect, *J. Geophys. Res.*, *114*, B01101, doi:10.1029/2007JB005326.

Stewart, K., and J. Foden (2003), Mesoproterozoic granites of South Australia, South Australia, *Tech. Rep. 2003/15*, Dept. of Primary Indust. and Resour., Adelaide, SA, Australia.

Swain, G., M. Hand, J. Teasdale, L. Rutherford, and C. Clark (2005a), Age constraints on terrane-scale shear zones in the Gawler Craton, southern Australia, *Precambrian Res.*, *139*(3–4), 164–180.

Swain, G., A. Woodhouse, M. Hand, K. Barovich, M. Schwarz, and C. Fanning (2005b), Provenance and tectonic development of the late Archaean Gawler Craton, Australia; U-Pb zircon, geochemical and Sm-Nd isotopic implications, *Precambrian Res.*, *141*(3–4), 106–136.

Swain, G., K. Barovich, M. Hand, G. Ferris, and M. Schwarz (2008), Petrogenesis of the st peter suite, southern australia: Arc magmatism and proterozoic crustal growth of the south australian craton, *Precambrian Res.*, *166*(1–4), 283–296.

Teasdale, J. (1997), Methods for understanding poorly exposed terranes: The interpretive geology and tectonothermal evolution of the western Gawler Craton, Ph.D. thesis, Univ. of Adelaide, Adelaide, SA, Australia.

ten Grotenhuis, S. M., M. R. Drury, C. J. Peach, and C. J. Spiers (2004), Electrical properties of fine-grained olivine: Evidence for grain boundary transport, *J. Geophys. Res.*, *109*, B06203, doi:10.1029/2003JB002799.

Thiel, S. (2008), Modelling and inversion of magnetotelluric data for 2-D and 3-D ithospheric structure, with application to obducted and subducted terranes, Ph.D. thesis, Univ. of Adelaide, Adelaide, SA, Australia.

Thiel, S., G. Heinson, and A. White (2005), Tectonic evolution of the southern Gawler craton, South Australia, from electromagnetic sounding, *Aust. J. Earth Sci.*, *52*, 887–896.

Thomas, J. L., N. G. Direen, and M. Hand (2008), Blind orogen: Integrated appraisal of multiple episodes of Mesoproterozoic deformation and reworking in the Fowler Domain, western Gawler Craton, Australia, *Precambrian Res.*, *166*(1–4), 263–282.

van der Hilst, R., B. Kennett, and T. Shibutani (1998), Upper mantle structure beneath Australia from portable array deployments, in *Structure and Evolution of the Australian Continent*, *Geodyn. Ser.*, vol. 26, edited by J. Bruan et al., pp. 39–57, AGU, Washington, D. C.

Wang, D., M. Mookherjee, Y. Xu, and S.-i. Karato (2006), The effect of water on the electrical conductivity of olivine, *Nature*, *443*(7114), 977–980.

Wannamaker, B. J., and A. G. Duba (1993), Electrical conductivity of San Carlos olivine along [100] under oxygen- and pyroxene-buffered conditions and implications for defect dquilibria, *J. Geophys. Res.*, *98*, 489–500.

Wannamaker, P., G. Jiracek, J. Stodt, T. Caldwell, V. Gonzalez, J. McKnight, and A. Porter (2002), Fluid generation and pathways beneath an active compressional orogen, the New Zealand Southern Alps, inferred from magnetotelluric data, *J. Geophys. Res.*, *107*(B6), 2117, doi:10.1029/2001JB000186.

Wessel, P., and W. Smith (1998), New,improved version of the Generic Mapping Tools released, *Eos Trans. AGU*, *79*, 579.

Xu, Y., B. T. Poe, T. J. Shankland, and D. C. Rubie (1998), Electrical conductivity of olivine, wadsleyite, and ringwoodite under upper-mantle conditions, *Science*, *280*(5368), 1415–1418.

G. Heinson and S. Thiel, School of Earth and Environmental Sciences, University of Adelaide, Adelaide SA 5005, Australia. (graham.heinson@adelaide.edu.au; stephan.thiel@adelaide.edu.au)